MEASUREMENT OF UNSTEADY PRESSURES AND FORCES ON AN ENGINE AND A WING/ENGINE COMBINATION INCLUDING JET SIMULATION

by

H. Triebstein, G. Schewe

German Aeronautical Research Establishment,
Institut for Aeroelasticity, Göttingen, FRG

H. Zingel, S. Vogel

Deutsche Airbus GmbH, Bremen, FRG

Abstract

Experimental investigations on the unsteady aerodynamic forces were performed on an ejector engine model and a wing/engine combination in the subsonic and transonic flow regimes. The experimental results were compared to theoretical results. The aim was to determine how well the commonly used mathematical aerodynamic models for flutter calculations correspond to the actual relationships observed on engines.

The investigations on the ejector engine demonstrated that linear lifting surface theory provides quite accurate unsteady aerodynamic forces. The effects of Mach number and reduced frequency are described correctly. For the wing/engine combination, the unsteady interference effect for engine oscillation on the lower side of the wing is strongly influenced by flow separation at the wing/pylon connection. In general, the unsteady aerodynamic forces on the wing are small and, at this order of magnitude, can be correctly calculated with linear lifting surface theory.

List of Symbols

A	m^2	cross section area
a	m/s	speed of sound
c_m		local pitch moment coefficient referred to 1/4
c_M		pitch moment coefficient
c_n		local normal force coefficient
c_N		normal force coefficient
c_p		pressure coefficient
Δc_p		pressure difference ($= c_{p,lower} - c_{p,upper}$)
d	m	engine inlet diameter
f	Hz	frequency
l	m	nacelle length, local chord
l_μ	m	reference chord
M	Nm	pitch moment
$\dot{m}$	kg/s	mass flow
M_∞		free stream Mach number
N	N	normal force
p	Pa	static pressure
p_t	Pa	engine model driving pressure
q	Pa	dynamic pressure
Re		Reynolds number
S	m^2	wing area
U_∞	m/s	free stream velocity
x,y,z	m	cartesian coordinates, parallel to the fuselage
$\bar{x},\bar{y},\bar{z}$	m	cartesian coordinates, parallel to the fuselage
$\tilde{x},\tilde{y},\tilde{z}$	m	cartesian coordinates, swept
α		angle of incidence
γ		damping ratio
ζ		mass flow coefficient
λ		taper ratio
Λ		aspect ratio
ν	m^2/s	kinematic viscosity
ϱ	kg/m	density
φ_{25}		sweep angle of 1/4-line
ω	1/s	circular frequency
ω^*		reduced frequency

51

1 Introduction

To improve the efficiency of aircraft engines and to reduce the noise emission, the bypass ratio of the engines has been increased in the past and will be further increased in the future. Future aircraft engines, for example the projected General Electric GE 90, or the CRISP project (counter rotating integrated shrouded propeller), will have a bypass ratio of 10 to 20. High bypass ratio engines result in a large engine diameter. Fig. 1 shows an Airbus A 300. The figure gives an impression of the engines dimensions in comparison to the aircraft.

Flutter calculations on aircraft with two large engines, located far in front of the wing leading edge, as shown in Fig. 1, have shown that above the wing bending frequency an engine pitch mode with a significant torsion of the outer wing exists, see Fig. 2. With increasing airspeed the frequencies of these two vibration modes come closer together and the damping curve passes the zero line. A flutter instability occures. Additionally, Fig. 2 shows the influence of the engine airforces on the flutter behaviour. The engine airforces reduce the generalized stiffness of the vibration modes with engine vibration constituents, by which the frequencies become smaller with increasing airspeed. The damping of the vibration modes with engine vibration constituents is increasing. The coupling terms of the generalized airloads are increased, by which the loss of damping is increased. The sum of these effects leads to a stronger flutter situation and to a flutter point at larger airspeed; see [1].

Present state of the art in the calculation of the engine airforces is to idealize the engine by a thicknessless flown through circular cylinder; see [2], [3].

Not represented are

o the nacelle profile,
o the cowling geometry,
o nonlinear interference effects due to flow separation in the connection areas between engine, pylon and wing,
o the fan jet and
o the primary jet.

Recently a cooperative programme between Deutsche Airbus GmbH and the German Aeronautical Research Establishment was carried out. Wind tunnel tests were performed in the Göttingen low speed wind tunnel and in the ONERA S2 transonic wind tunnel on an isolated engine model and in the Göttingen low speed wind tunnel on a wing/engine combination. The aim was to determine how well the commonly used mathematical aerodynamic models for flutter calculations correspond to the actual relationships on engines and wing/engine combinations. The present paper gives a view of the results. Some more details are discussed in [4] and [5].

2 Experimental Investigations on the Isolated Engine Model

2.1 Test Arrangement

Present state of the art of engine simulation in wind tunnel are the turbine powered simulator models, by which the aerodynamic parameters like the inlet mass flow coefficient and the exhaust nozzle impuls are well approximated. The TPS-models, however, are very sensitive against vibrations so that they could not be used for investigations on harmonically oscillating engine models. Therefore the conventional ejector principle was used for jet simulation.

The wind tunnel model and the principle of the test arrangement are shown in Fig. 3. The engine model is a 1:13 scaled General Electric CF6-50 engine. Pressurised air (m_1) is led into the engine model with a pressure of up to 20 bar and is blowing out through Laval nozzels. The pressurised air entering the bypass channel sweeps away the air entering the engine through the inlet and increases in this way the mass flow through the inlet m_2. The mass flow at the bypass exhaust nozzle becomes

$$\dot{m}_5 = \dot{m}_1 + \dot{m}_2 \qquad (1)$$

The engine model is also designed to generate a primary jet. In this case the primary stream exhaust nozzle mass flow was added to the bypass exhaust nozzle mass flow ($\dot{m}_5 = \dot{m}_{5,M} + \dot{m}_{5,K}$). The bypass ratio $\dot{m}_{5,M}/\dot{m}_{5,K}$ results to about 5 and is about the value of the real engine.

The engine model is fixed by a sting in an electro-hydraulic exciter. The model can be driven to harmonical pitch vibrations.

The engine model is instrumented with a piezo-electrical balance, which is mounted between sting and engine. Piezo-electrical balances recently were used successfully by G. Schewe [6], [7], especially for the measurement of unsteady airloads. A total of 33 pressure transducers are mounted in three nacelle sections (see Fig. 3). The engine model vibrations are measured by four accelerometers in addition to a rotation angle pick-up.

To determine the mass flows through the engine model, calibration measurements were performed in the Göttingen calibration tank. Fig. 4 shows the dimensionless mass flow coefficients

$$\xi_2 = \frac{\dot{m}_2}{\rho_\infty \, a_\infty \, M_\infty \, A_2} \qquad (2a)$$

at the engine inlet and

$$\xi_5 = \frac{\dot{m}_5}{\rho_\infty \, a_\infty \, M_\infty \, A_2} \qquad (2b)$$

at the exhaust nozzle versus the free stream Mach number M_∞ and for different driving pressures p_t. ρ_∞ is the free stream density, a_∞ is the speed of sound and A_2 is the inlet cross section area. With increasing Mach number the effectiveness of the ejector decreases. At Mach numbers $M_\infty > 0,6$ the inlet mass flow is no more increased by increasing driving pressure. Whilst the inlet mass flow coefficient ξ_2 of the aircraft is not reached for low Mach numbers and is crude approximated for cuise conditions, the exhaust nozzle mass flow coefficient ξ_5 is well approximated.

2.2 Steady Airloads

First, the steady airloads will be discussed. Fig. 5 shows the measured pressure distribution $c_p(x/l)$ of section 2 for different mass flow coefficients ξ_2 and ξ_5 and for different Mach numbers M_∞.

The pressure coefficient is defined as

$$c_p(x/l) = \frac{p(x/l) - p_\infty}{q_\infty} \qquad (3)$$

with the static pressure $p(x/l)$, the free stream static pressure p_∞ and the free stream dynamic pressure q_∞. The pressure distributions of the undriven engine ($p_t = 0$ bar) at subsonic Mach numbers $M_\infty < 0,8$ are characterised by a suction peak at the nacelle leading edge. A second, smaller suction peak at $x/l = 0,2$ is caused by a discontinuity of the nacelle profile. The pressures on the nacelle inner side are relatively high. This is due to the throttling caused by the necessary installations in the bypass channel.

The increase of the Mach number from $M_\infty = 0,18$ to $M_\infty = 0,5$ leads to only a small increase of the suction peaks on the nacelle outer side and to an increase of the pressures on the inner side. At Mach number $M_\infty = 0,8$ supersonic flow locally occures.

The increase of the inlet mass flow coefficient ξ_2 at low Mach number $M_\infty = 0,18$ results in a shift of the stagnation point on the inner side of the nacelle towards the leading edge. Consequently the suction peak on the outer engine side is decreased and now a suction peak on the inner side is built up.

At the larger Mach number $M_\infty = 0,5$ the inlet mass flow coefficient ξ_2 is nearly unchanged with increasing driving pressure. The pressure distribution is only slightly influenced on the inner side of the nacelle. The increasing exhaust nozzle mass flow nearly does not influence the nacelle pressure distribution.

At transonic Mach number $M_\infty = 0,8$ the increasing driving pressure causes a stronger throttling of the flow through. This results in a pressure increase on the nacelle inner side and a slightly change of the supersonic flow region.

The normal force coefficient slope $c_{N,\alpha}$ and the pitch moment coefficient slope $c_{M,\alpha}$ were calculated with a steady panel method on the basis of potential flow theory [8]. The normal force coefficient slope is defined as

$$c_{N,\alpha} = \frac{N_\alpha}{q_\infty \, d_2 \, l} \qquad (4)$$

with the normal force slope N_α, the nacelle length l and the inlet diameter d_2. The pitch moment coefficient slope is

$$c_{M,\alpha} = \frac{M_\alpha}{q_\infty \, d_2 \, l^2} \qquad (5)$$

with the pitch moment slope M_α referred to the engine model pitch axis. They are plotted in Fig. 6 against the inlet mass flow coefficient ξ_2. The calculation method [8] is able to consider the nacelle profile, the inlet mass flow and the exhaust nozzle mass flow separately, and the jet.

With increasing inlet mass flow coefficient ξ_2 the normal force coefficient slope $c_{N,\alpha}$ and the pitch moment coefficient slope $c_{M,\alpha}$ are increasing linearly. A systematically change of the exhaust nozzle mass flow coefficient ξ_5 results in the assessment that this parameter does not affect the engine airloads significantly. The normal force coefficient slope $c_{N,\alpha}$ and the pitch moment coefficient slope $c_{M,\alpha}$ were calculated with the doublet-lattice method [2]. The engine model was idealized by an approximated circual cylinder. The calculated values are somewhat smaller than the values calculated with the steady panel method [8]. This is due to the simplified engine geometry in the doublet-lattice calculation.

The measured pressure distributions were integrated to derive the normal force and pitch moment coefficient slopes $c_{N,\alpha}$ and

$c_{M,\alpha}$. Basis was only the cross section 2. The pressure distribution in circumfencional direction was approximated by a simple cosine distribution. Measurement and calculation are in good coincidence.

Taking into account the interference effect of the engine sting in the doublet-lattice calculation gives in particular a larger normal force slope. The force measurement, by use of the piezo balance, which includes the interference effect, gives corresponding larger normal force and pitch moment coefficient slopes compared to the integrated pressure distribution.

2.3 Unsteady Airloads

The unsteady airloads were measured on the harmonically pitching engine model. The unsteady pressure distributions

$$re\ c_p(x/l) + i\ im\ c_p(x/l) = \frac{re\ p(x/l)}{q_\infty} + i\frac{im\ p(x/l)}{q_\infty} \quad (6)$$

are plotted in Fig. 7 for different Mach numbers M_∞ and different mass flow coefficients ζ_2 and ζ_5. At subsonic Mach numbers $M_\infty = 0,18$ and $M_\infty = 0,5$ the unsteady pressure distributions are characterised by a marked suction peak near the nacelle leading edge on the outer side. With increasing inlet mass flow coefficient ζ_2 the pressure peak on the inner side of the nacelle increases, whilst the suction peak on the outer side decreases. With increasing Mach number the pressure peak on the inner side increases, but this is an effect of the increased inlet mass flow coefficient ζ_2, too. At transonic Mach number $M_\infty = 0,8$ a pronounced suction peak occures at $x/l = 0,1$, which corresponds to the maximum pressure slope $\partial c_p/\partial x$ of the steady pressure distribution (see Fig. 5). The supersonic flow region is responding sensitively to small changes of the mass flow parameters ζ_2 and ζ_5.

In the same way as the steady pressure distributions in Chapter 2.2 the unsteady pressure distributions were integrated to unsteady normal force coefficients $c_{N,\alpha}$ and pitch moment coefficients $c_{M,\alpha}$, which are plotted in Fig. 8 against the reduced frequency

$$\omega^* = \frac{2\pi\ f\ l}{U_\infty} \quad (7)$$

for different mass flow coefficients ζ_2 and ζ_5. The Mach number is $M_\infty = 0,18$. With increasing reduced frequency $\omega*$ the real parts of the normal force coefficient and the pitch moment coefficient increase slightly. The normal force and pitch moment coefficients increase in real and imaginary part with increasing mass flow coefficients is evident.

The unsteady airloads of the engine model were calculated using a Kernel function-method of J.J. Angelini [3]. The engine model geometry was approximated by a flowing through circular cylinder, this having the mass flow parameters $\zeta_2 = \zeta_5 = 1$. The comparison of measurement and calculation shows that the increase of the real parts with increasing reduced frequency are well approximated, but the real parts are underpredicted as a whole.

The influence of the Mach number M_∞ on the unsteady normal force and pitch moment coefficients is plotted in Fig. 9. In this case the forces and moments were measured with the piezo balance. The inlet mass flow coefficient is approximately constant $\zeta_2 = 0,4$, whilst the exhaust nozzle mass flow coefficient changes with increasing driving pressure p_t. With increasing Mach number, the real part of the normal force coefficient is slightly increasing. The real part of the pitch moment coefficient is nearly constant, but shows a certain scatter at transonic Mach numbers.

The unsteady airloads were calculated by use of the doublet-lattice method. The interference of the sting is included in the calculation. The Mach number dependence of the unsteady airloads is well approximated by the calculation. The calculated unsteady airloads in this case are larger than the measured one, because the interference effect of the engine model sting is overpredicted.

3 Experimental Investigations on the Wing/Engine Combination

3.1 Test Arrangement

After the steady and unsteady airloads were investigated on the isolated engine, now the wing will be introduced in the considerations. Both the influence of the wing on the steady and unsteady airloads of the engine, and the influence of the engine on the steady and unsteady airloads of the wing will be discussed.

The test arrangement in the Göttingen 3m x 3m low speed wind tunnel is shown in Fig. 10. With an electro-hydraulic exciter the engine can be driven to harmonical pitch vibrations, whilst the wing is resting. The engine also can be fixed mechanically, so that the wing/engine combination can be driven to harmonical pitch vibrations around a swept rotation axis by use of a second hydraulic actuator at the wing root. Fig. 11 gives an impression of the test arrangement in the wind tunnel.

The instrumentation of the engine model was nearly the same as for the measurements on the isolated engine. The wing was instrumented with a total of 120 pressure transducers in four sections (see Fig.10), six accelerometers and a piezo-balance at the wing root.

54

3.2 Steady Airloads

Again the steady airloads will be considered first. In Fig. 12 the steady pressure distribution $c_p(x/l)$ on the wing is plotted for different mass flow coefficients ζ_2 and ζ_5. For all mass flow coefficients it can be noticed that the stagnation point is shifted towards the wing leading edge, passing the sections from the root towards the tip. Due to the influence of increasing jet strength ζ_5, the stagnation point is shifted towards the leading edge in all sections considered. This results in a decrease of the suction on the wing upper side. At the same time the suction on the lower side is increased. The total result is a decrease of the normal force coefficient c_N of the wing and an increase of the nose-heavy pitch moment coefficient c_M, as plotted in Fig. 13. The normal force coefficient of the wing is defined as

$$c_N = \frac{N}{q_\infty\, S} \tag{8}$$

with the area of the half wing S. The pitch moment coefficient referred to the pitch axis is defined as

$$c_M = \frac{M}{q_\infty\, S\, l_\mu} \tag{9}$$

with the reference wing chord l_μ .

The influence of the engine on the quasisteady pressure distribution of the wing $c_{p,a}(x/l)$ is shown in Fig. 14. Due to the influence of the jet strength ζ_5 the quasisteady pressure on the lower surface increases significantly, whilst the quasisteady pressure distribution on the upper surface is nearly unaffected. This results in an increase of the local quasisteady normal force coefficient $c_{n,a}(\bar{y}/s)$ and an increase of the local tail-heavy pitch moment coefficient $c_{m,a}(\bar{y}/s)$ with increasing jet strength ζ_5, as plotted in Fig. 15. The comparison of the measurement with a doublet-lattice calculation gives a well coincidence.

In Fig. 16 the influence of the wing on the quasisteady pressure distribution $\Delta c_{p,a}(x/l)$ on the engine is plotted. The lift force, generated in section 6, is decreased due to the presence of the wing. Systematical theoretical investigations have shown that the influence of the wing on the engine is strongly affected by the location of the engine relative to the wing. The doublet-lattice calculation of the engine pressure distribution shows a satisfactory coincidence with the measurement.

3.3 Unsteady Airloads

The unsteady airloads were investigated on the harmonically oscillating engine and the wing in rest. The unsteady pressure distributions re $c_p(x/l)$ and im $c_p(x/l)$ on the wing are plotted for two sections and at different reduced frequencies $\omega*$ in Fig. 17. The unsteady pressure distribution on the lower surface differs from that on the upper surface remarkebly. Pronounced minima and maxima are investigated at different locations inboard and outboard of the pylon. The wave character of the unsteady pressure distributions are nearly unaffected by the reduced frequency $\omega*$ of the engine pitch vibration. Thus the character of the unsteady pressure distributions is not the result of the harmonically oscillating engine downwash area. A local flow separation occures at the connection between wing and pylon, which is the reason for the odd unsteady pressure distribution. Fig. 18 shows an oil flow picture and the corresponding wall streamlines. Flow separation is visible in the vicinity of the pylon, and is coating the pressure measurement sections.

The integration of the unsteady pressure distributions gives unsteady local normal force coefficients re $c_n(\bar{y}/s)$ and im $c_n(\bar{y}/s)$ and unsteady local pitch moment coefficients re $c_m(\bar{y}/s)$ and im $c_m(\bar{y}/s)$, which are plotted in Fig. 19. The influence of the oscillating engine on the unsteady airloads of the wing are not very pronounced. The unsteady local normal force coefficients and pitch moment coefficients are very small. A calculation of the unsteady pressure distribution, using the doublet-lattice method, can not, of course, represent the measured unsteady pressures, as shown in Fig. 16. But the calculated local unsteady airloads are in the same order than the measured one.

The unsteady pressures on the oscillating engine are nearly unaffected by the presence of the wing at rest, because the unsteady airloads on the wing are of small quantity.

4 Conclusion and Outlook

Experimental investigations of the unsteady airloads on an engine model and a wing/engine combination had been carried out. The aim was to find out, whether the usually used flown through circular cylinders as mathematical models in flutter calculations are appropriate to describe the real flow conditions on the engine and the wing/engine combination.

The wind tunnel tests on the harmonically oscillating isolated engine have shown that the pressure distributions are significantly affected by compressibility effects like transonic flow, but the airloads are nearly unchanged. With increasing inlet mass flow coefficient the unsteady airloads increase, whereas the direct influence of the jet strength is small. The unsteady airloads increase with increasing reduced frequency.

The calculated unsteady airloads are smaller than the measured ones at identical in-

let mass flow coefficient. This means that the calculated unsteady airloads are in well coincidence with the measurement, when the inlet mass flow is throttled, as it is the case in the cruise condition of the aircraft.

The wind tunnel tests on the wing/engine model with the engine in harmonically pitch oscillation have shown that the unsteady pressures on the wing lower side are strongly affected by a complex flow separation in the region of the wing/pylon connection. The magnitudes of the unsteady airloads are small, and they are calculated in the right order by the doublet-lattice method.

Finally, it can be concluded that the unsteady airloads of a wing/engine combination, as they are necessary for flutter calculations, are satisfactory predicted by the usually used doublet-lattice method, provided that the engine is of presently used type with moderate bypass ratio. Future engine developments will lead to larger engine diameters, so that the influence of the engine aerodynamics on the aircraft flutter behaviour will increase. Consequently the unsteady engine airforces and their interference effects on the wing have to be considered in the flutter calculation with more accuracy.

5 References

[1] Zimmermann, H., Vogel, S.: Influence of Main Design Parameters on Flutter Behaviour for Aircraft Configurations with Heavy Concentrated Masses. AGARD CP. No. 354 (1983) pp. 6-1 to 6-11.

[2] Albano, E., Rodden, W.P.: A Doublet-Lattice Method for Calculating Lift Distributions on Oscillating Surfaces in Subsonic Flow. AIAA-Journal Vol. 7 (1969) pp. 279-285.

[3] Angelini, J.J., Chopin, S., Destuynder, R.: Forces aerodynamiques instationaires par les vibrations aeroelastiques d'un reacteur en nacelle. La Recherche Aerospatiale, No. 1974-4 (1974) pp. 209-219.

[4] Zingel, H., Vogel, S., Triebstein, H., Schewe, G., Katzer, E.: Experimentelle und theoretische Untersuchung der stationären und instationären Luftkräfte an Strahltriebwerken. DGLR-Jahrbuch 1988 I, 88-059 (1988), S. 323-332.

[5] Zingel, H., Jajes, U., Vogel, S.: Bestimmung instationärer Triebwerksluftkräfte für die Anwendung bei Flatteruntersuchungen. MBB, internal report, TE 234-B27/89, 1989.

[6] Schewe, G.: Mehrkomponentenwaage bestehend aus piezoelektrischen Kraftelementen für einen Hochdruckwindkanal. Techn. Messen 49 (1982), H. 12.

[7] Schewe, G.: Beispiele für Kraftmessungen im Windkanal mit piezoelektrischen Mehrkomponenten-Meßelementen. Z. Flugwiss. 14, H.12 (1990) S. 32-37.

[8] Ehrmann, M., Klevenhusen, K.D., Rudolph, K,. Burgsmüller, W.: Computation of Engine-Airframe Interference Flows at Subsonic and Transonic Speed / Comparison with Flight and Windtunnel Tests. ICAS-84-2.10.1. (1984).

Fig. 1: Airbus A300

Fig. 3: Engine model

$$\zeta = \frac{\dot{m}}{\rho_\infty M_\infty a_\infty A_2}$$

○ $p_t = 20$ bar   × $p_t = 0$ bar   ● aircraft
□ $p_t = 10$ bar   △ $p_t = 1$ bar
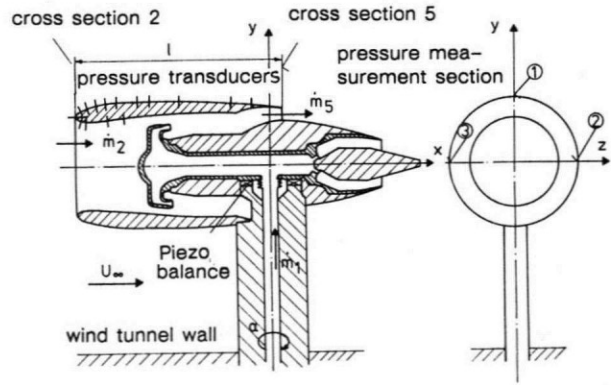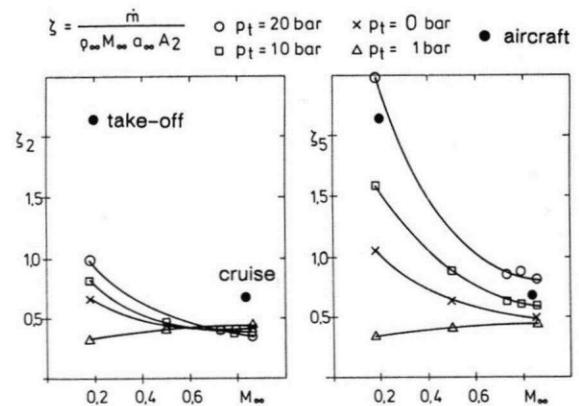
Fig. 4: Influence of Mach number M_∞ on the mass flow coefficients ξ_2 and ξ_5

—— without engine airloads
—·— with engine airloads
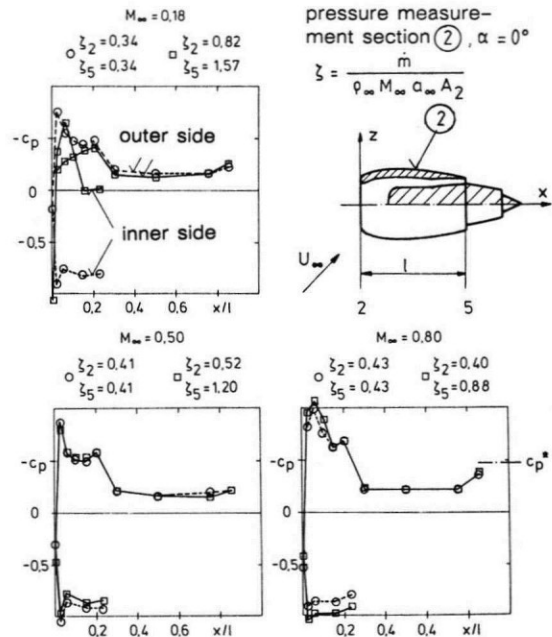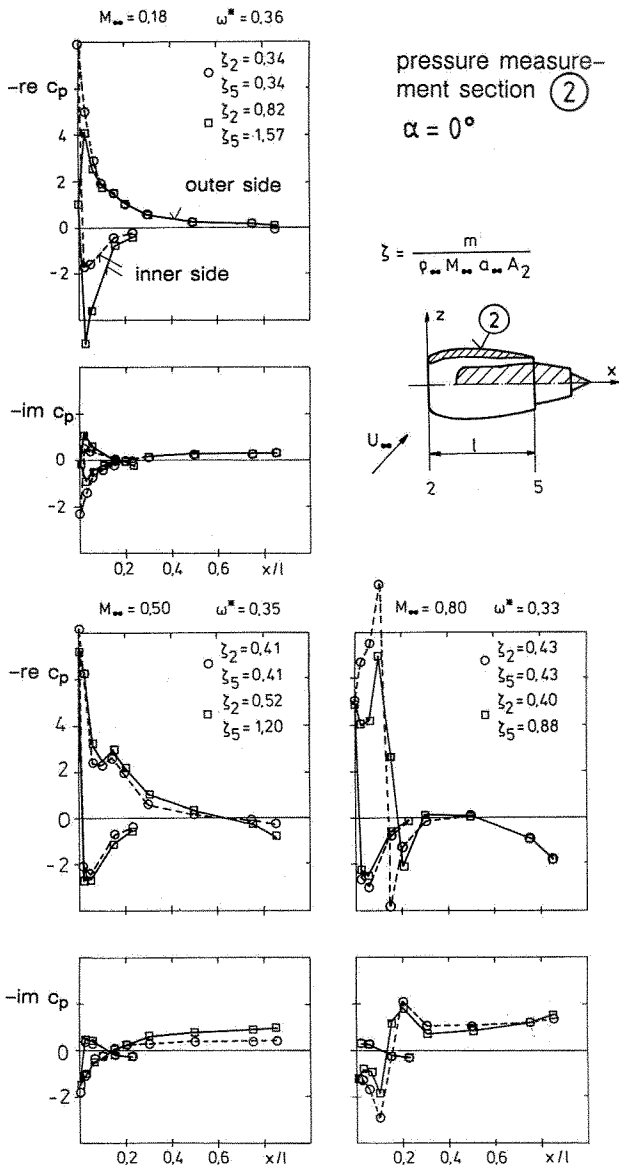

Fig. 2: Influence of the engine airforces on the flutter behaviour

Fig. 5: Steady pressure distribution $c_p(x/l)$; influence of Mach number M_∞ and mass flow coefficients ξ_2 and ξ_5
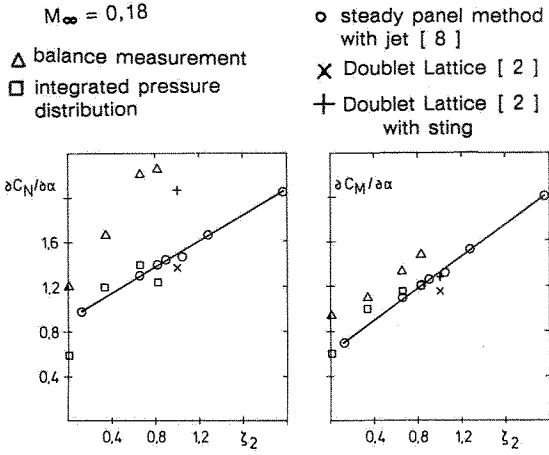
Fig. 6: Normal force slope $c_{N,\alpha}$ and pitch moment slope $c_{M,\alpha}$ versus inlet mass flow coefficient ξ_2

Fig. 7: Unsteady pressure distribution re $c_p(x/l)$ and im $c_p(x/l)$, influence of Mach number M_∞

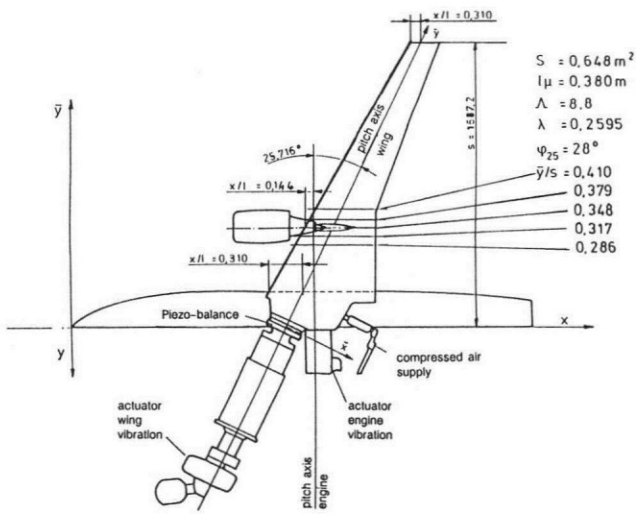Fig. 8: Unsteady normal force coefficient re c_N and im c_N and pitch moment coefficient re c_M and im c_M versus reduced frequency ω^*; influence of mass flow coefficients ξ_2 and ξ_5
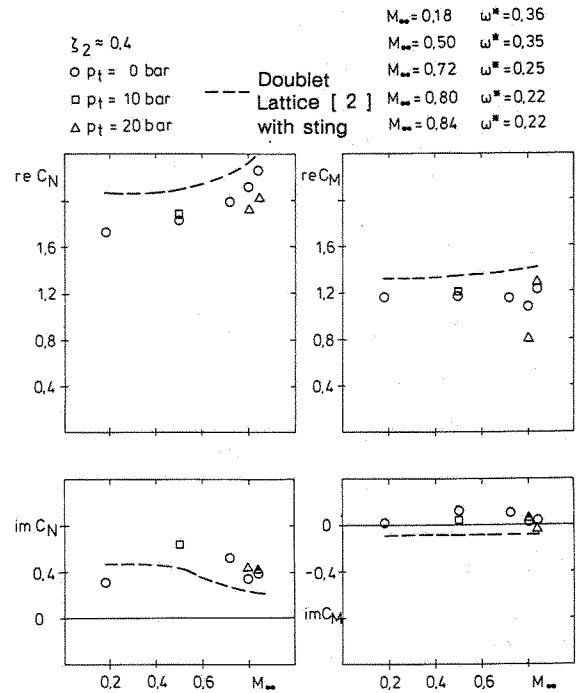
Fig. 9 Unsteady normal force coefficient re c_N and im c_N and pitch moment coefficient re c_M and im c_M versus Mach number M_∞

Fig. 10: Test arrangement, schematical

○ $\zeta_2 = 0.341$; $\zeta_5 = 0.341$
× $\zeta_2 = 0.668$; $\zeta_5 = 0.903$
◇ $\zeta_2 = 0.819$; $\zeta_5 = 1.276$
▨ $\zeta_2 = 0.983$; $\zeta_5 = 1.936$

$M_\infty = 0.18$; $\alpha = 3^\circ$

Fig. 12: Steady pressure distribution $c_p(x/l)$ on the wing, influence of the jet strength ξ_5
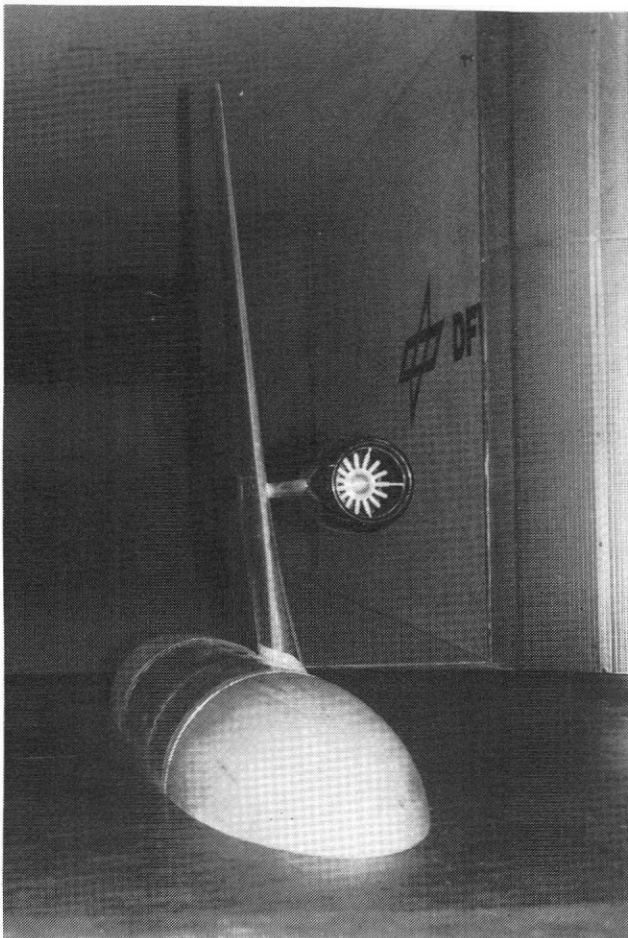
Fig. 11: Wind tunnel model in the Göttingen low speed wind tunnel
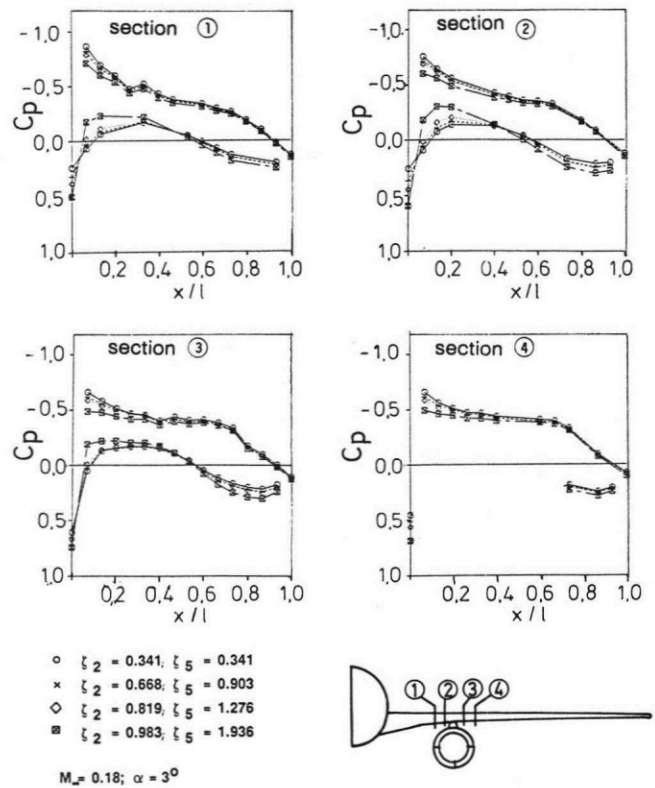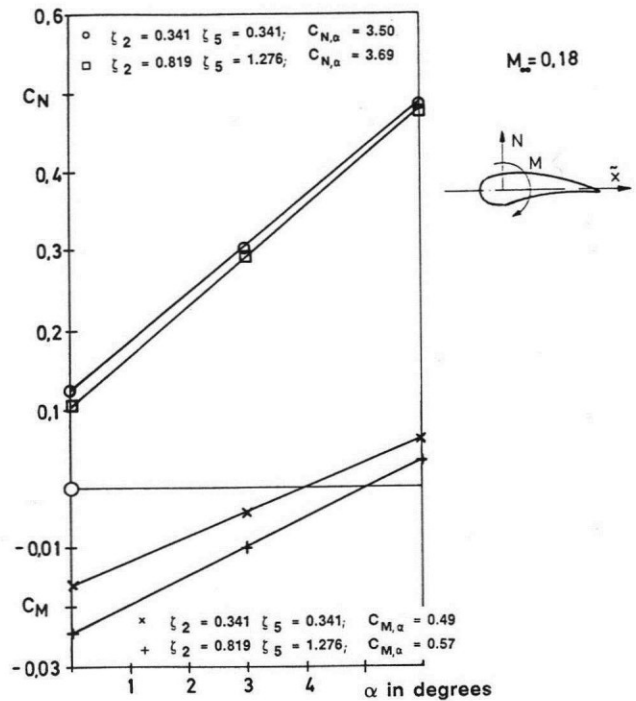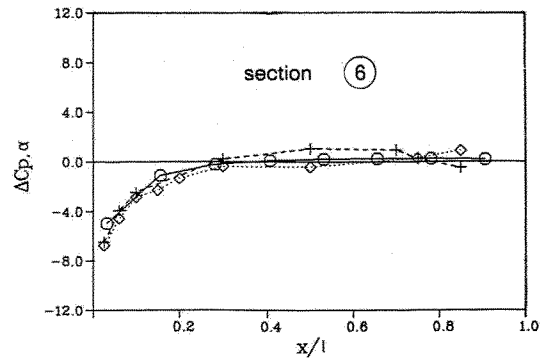

Fig. 13: Steady normal force and pitch moment coefficient $c_N(\alpha)$ and $c_M(\alpha)$; influence of jet strength ξ_5
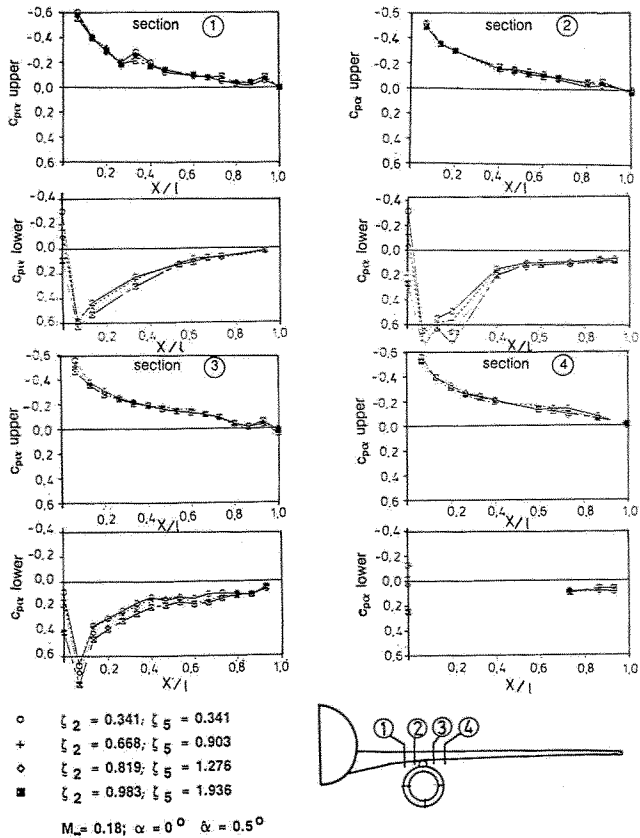
Fig. 14: Quasisteady pressure distribution $c_{p,\alpha}(x/l)$ on the wing, influence of the jet strength ξ_5

Legend for Fig. 14:

o	$\zeta_2 = 0.341$;	$\zeta_5 = 0.341$
+	$\zeta_2 = 0.668$;	$\zeta_5 = 0.903$
◇	$\zeta_2 = 0.819$;	$\zeta_5 = 1.276$
✹	$\zeta_2 = 0.983$;	$\zeta_5 = 1.936$

$M_\infty = 0.18$; $\alpha = 0°$; $\hat{\alpha} = 0.5°$
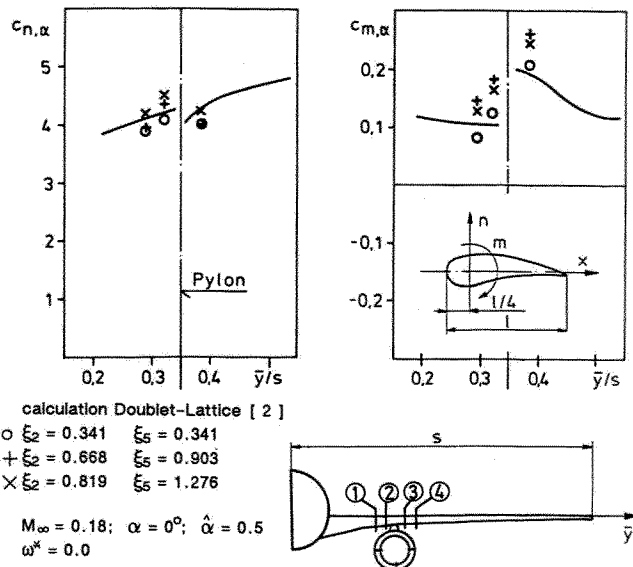
Fig. 15: Quasisteady normal force and pitch moment coefficient $c_{n,\alpha}(\bar{y}/s)$ and $c_{m,\alpha}(\bar{y}/s)$; influence of the jet strength ξ_5
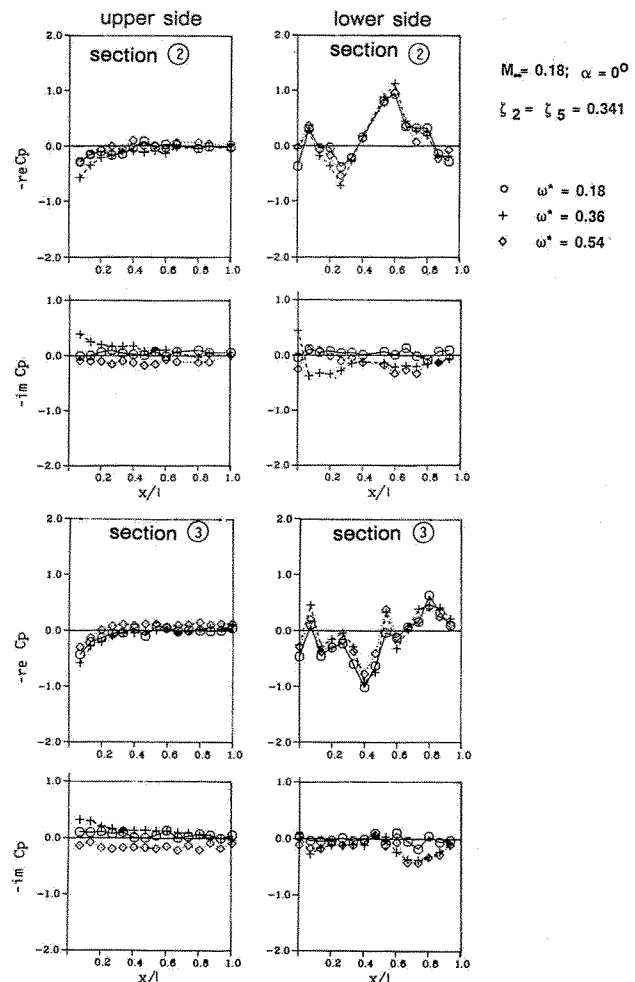
calculation Doublet-Lattice [2]

o	$\xi_2 = 0.341$	$\xi_5 = 0.341$
+	$\xi_2 = 0.668$	$\xi_5 = 0.903$
×	$\xi_2 = 0.819$	$\xi_5 = 1.276$

$M_\infty = 0.18$; $\alpha = 0°$; $\hat{\alpha} = 0.5$
$\omega^* = 0.0$

◇ measurement $\xi_2 = \xi_5 = 0.341$; $\alpha = 0°$; $\hat{\alpha} = 1.0$; isolated engine
+ measurement $\xi_2 = \xi_5 = 0.341$; $\alpha = 0°$; $\hat{\alpha} = 0.5$
o calculation Doublet-Lattice [2]

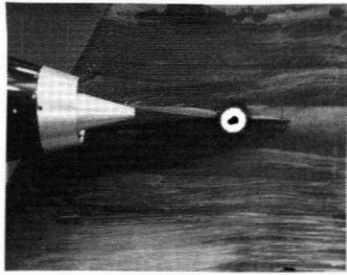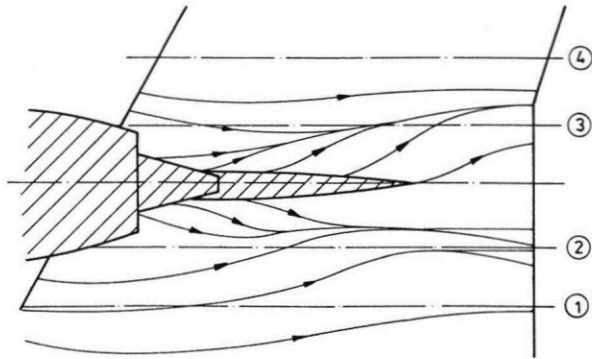$M_\infty = 0.18$
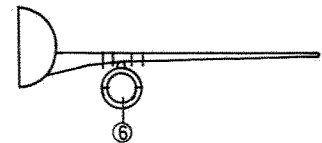
Fig. 16: Quasisteady pressure distribution $\Delta c_{p,\alpha}(x/l)$ on the engine

$M_\infty = 0.18$; $\alpha = 0°$
$\zeta_2 = \zeta_5 = 0.341$

o	$\omega^* = 0.18$
+	$\omega^* = 0.36$
◇	$\omega^* = 0.54$

Fig. 17: Unsteady pressure distribution re $c_p(x/l)$ and im $c_p(x/l)$ on the wing; influence of the reduced frequency ω^*
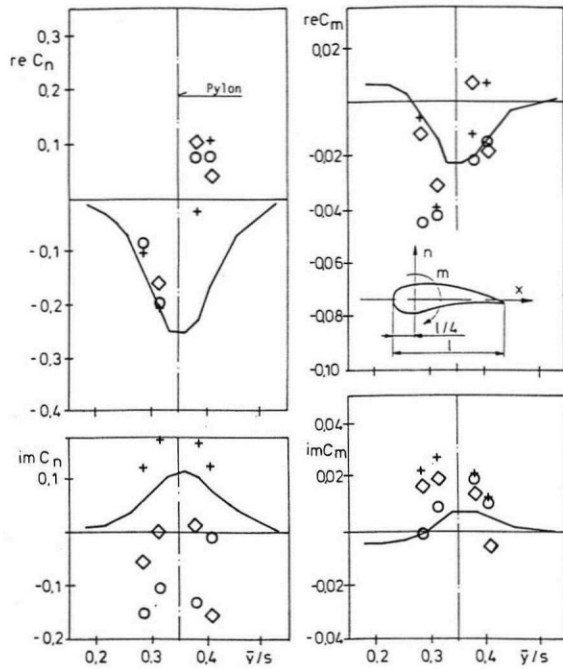
60

oil flow picture
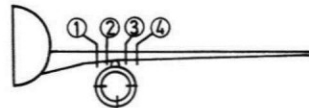

wall stream lines

Fig. 18: Oil flow picture and wall stream lines on the wing; $M_\infty = 0,18$; $\alpha = 0°$; $\xi_2 = \xi_5 = 0,341$

— calculation Doublet–Lattice $\omega^* = 0.36$
O $\omega^* = 0.18$
+ $\omega^* = 0.36$
◇ $\omega^* = 0.54$

$M_\infty = 0.18$; $\alpha = 0°$; $\xi_2 = \xi_5 = 0.341$

Fig. 19: Unsteady normal force and pitch moment distribution re $c_n(\bar{y}/s)$, im $c_n(\bar{y}/s)$, re $c_m(\bar{y}/s)$ and im $c_m(\bar{y}/s)$; influence of the reduced frequency ω^*

61